Re-entry Shape Optimisation Using the Axisymmetric Analogue Method with Modified Newtonian Technique Resolved Inviscid Flowfield

Brchnelová, M.; Mooij, E.

DOI
10.2514/6.2021-0171

Publication date
2021

Document Version
Final published version

Published in
AIAA Scitech 2021 Forum

AIAA SciTech Forum
11–15 & 19–21 January 2021, VIRTUAL EVENT
AIAA Scitech 2021 Forum

10.2514/6.2021-0171

Re-entry Shape Optimisation Using the Axisymmetric Analogue Method with Modified Newtonian Technique Resolved Inviscid Flow Field

Michaela Brchnelova* and Erwin Mooij†
Delft University of Technology, Faculty of Aerospace Engineering,
Kluyverweg 1, 2629 HS Delft, The Netherlands

Re-entry shape and trajectory optimisation studies typically require hundreds to thousands of flow solutions to resolve the heat transfer and skin friction. Due to the fact that full CFD simulations and even Euler simulations are typically very expensive, this work presents a development of a much simpler technique, in which the modified Newtonian approximation is coupled with the axisymmetric-analogue-based viscous method. Afterwards, the developed technique is applied to the shape optimisation study of the DART module originally conducted by Sudmeijer and Mooij in 2002. Large differences in heat fluxes are observed mainly owing to the fact that the present method estimates the transition region from approximate transition criteria while the original study assumes the transition point to be fixed at the interface between the cone and the flare. This emphasises the sensitivity of design optimisation studies on delicate parameters such as the location of transition, which typically cannot be accurately predicted during the conceptual phase. Finally, the limitations of the current method are identified and the areas in which the technique will be improved further are outlined.

I. Introduction

Accurate full 3D solutions of hypersonic aerodynamics using computational fluid dynamics (CFD) are typically very computationally demanding. Despite the fact that the computational power availability has been growing rapidly, for studies, such as shape and trajectory optimisation for re-entry, full CFD solutions often cannot be afforded. Thus, aerodynamic prediction methods can be used instead to at least approximately indicate the ideal design space for further refinement for which CFD simulations can be used afterwards.

A potential application is the design of re-entry capsules, where in the conceptual design phase many configurations are studied in combination with the trajectory to be flown. It would be impractical to use advanced CFD codes to do a thorough design-space exploration, but it would also not suffice when the applied approximations steer the designers in the wrong direction. In Ref. 1 the shape optimisation of biconic entry capsules is studied, using a modified Newtonian method to calculate the aerodynamics, and approximate expressions to get an indication of the heat flux in the stagnation point, on the frontal conic section, and on the flare. However, because a proper verification of the heat-flux results is lacking in combination with the potential low fidelity, the need for a more accurate methodology to support the conceptual design of entry vehicles has arisen.

One such aerodynamic prediction technique is the method of the axisymmetric analogue, which allows the use of the approximate axisymmetric laminar and turbulent heating relations to be applied to full 3D geometries. This method has been in use since 1961 when it was developed by Cooke.[2] It has also been applied to Space-Shuttle-like geometries and repeatedly shown a good agreement with the experimental data,[3–6] with relatively small computational efforts compared to viscous CFD. The translation to 3D takes form in terms of a so-called metric coefficient, expressing the local spreading of the streamlines, determination methods for which have been proposed by Hamilton[7] and Parzhikar.[8]

*MSc Graduate Student, Section Aerodynamics, m.brchnelova@gmail.com, Student Member AIAA.
†Associate Professor, section Astrodynamics and Space Missions, e.mooij@tudelft.nl, Associate Fellow AIAA.

In 2009, Hamilton showed how well the use of the axisymmetric analogue can match the full CFD data for a wide range of scales and flow regimes with the Space Shuttle geometry.[7] There, he used, as is now common, the axisymmetric analogue technique with an Euler CFD solution as an input inviscid field. Whereas Euler solutions are definitely much less expensive compared to full viscous CFD, computing the Euler solutions at each iteration while exploring the design space for which hundreds to thousands of runs must be made can still be computationally demanding. Additionally, in the initial stages of a design study, the Euler solutions might provide an accuracy which is unnecessarily high given the computational demands.

Several techniques can be used to estimate the inviscid flow field in hypersonic flow. The most straightforward of those, which, unlike the rest, is not limited to simple or axisymmetric geometries, is the modified Newtonian technique. It estimates a surface pressure coefficient on the windward side as a function of the local surface inclination only. While the physics behind this technique is close to non-existent, the modified Newtonian method has been repeatedly shown to result in an agreement, which might be sufficient for at least a coarse optimisation of shape and trajectory.[9]

Thus, the focus of this work is to explore whether a simple modified Newtonian technique could act as a sufficiently accurate representation of the inviscid field for the axisymmetric analogue technique, and whether the resulting errors are acceptable for the first stages of re-entry design optimisation studies. Due to the limitations of the Newtonian technique, this optimisation can be performed for the windward side only. If the found errors are within an acceptable range, significant computational resources can be saved such studies in the future.

The layout of this paper is as follows. Section II introduces the theory behind the aerothermodynamic prediction model, with some numerical issues addressed in Sec. III. The validation of the proposed model is covered in Sec. IV, where the obtained results are compared with a number of related test cases published in literature. Results concerning the computational performance are also presented. As an example application, in Sec. V the shape optimisation of a ballistic, biconic entry capsule is discussed, the results of which are compared with those of an earlier study.[1] After a discussion in Sec. VI, Sec. VII concludes this paper with final remarks and an outlook for future research related to the present method.

II. Theory

In this section, the theory behind the aerodynamic simulation tool developed is discussed in detail. The assumed coordinate system for the aerodynamic relations applied is shown in Fig. 1. All the geometries presented below conform to this coordinate system.

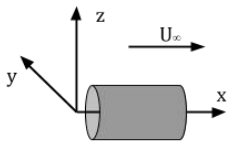

Figure 1. The coordinate system used for the aerodynamic simulations.

A. Approximate Inviscid Flow Field with Newtonian Theory

The modified Newtonian technique is probably the most simple rule-of-thumb method in hypersonic aerodynamics despite the lack of physics behind it. It has been repeatedly shown to yield a relatively good agreement with experimental data and CFD for a negligible computational cost.[9] To compute the pressure according to the modified Newtonian method, the maximum pressure coefficient has to be determined from the freestream Mach number M_∞ and ratio of specific heats γ,

$$\frac{p_{O_2}}{p_\infty} = \left[\frac{(\gamma+1)^2 M_\infty^2}{4\gamma M_\infty^2 - 2(\gamma-1)}\right]^{\frac{-\gamma}{\gamma-1}} \left[\frac{1-\gamma+2\gamma M_\infty^2}{\gamma+1}\right] \tag{1}$$

and then, for a panel i on the vehicle with the angle θ with respect to the freestream, the pressure coefficient C_p is given by

$$C_{p_i} = C_{p_{max}} \sin^2 \theta_i \tag{2}$$

with the maximum pressure coefficient determined from Eq. 1,

$$C_{p_{max}} = \frac{2}{\gamma M_\infty^2}\left(\frac{p_{O_2}}{p_\infty} - 1\right) \tag{3}$$

Thus the inviscid pressure field depends solely on the incidence angle of the local geometry. The velocity field (in terms of the Mach number) can then be resolved from the pressure field with the resulting velocity component aligned with the local geometry (at angle of θ_i with respect to freestream). It is obvious from Eq. (2) that this method only works for the windward regions with a positive pressure coefficient - that is, if the dot product of the outward surface normal $\hat{\mathbf{n}}$ with the velocity vector is negative,

$$\begin{pmatrix} V_x & V_y & V_z \end{pmatrix}^{\mathrm{T}} \cdot \begin{pmatrix} n_x & n_y & n_z \end{pmatrix}^{\mathrm{T}} < 0 \tag{4}$$

The shadow regions are defined as an entity for which Eq. (4) is either 0 or negative. In case the modified Newton method is used, C_p can be said to be approximately proportional to the negative inverse of the square of Mach number according to the data presented in Ref. 10. The modified Newtonian technique can, in this way, be used to very roughly approximate boundary layer edge properties.

B. Boundary Layer Edge Analysis

Apart from the boundary layer edge properties estimated from the modified Newtonian technique, the calculation of the heat flux and skin friction via the axisymmetric analogue also requires the reference boundary layer values of viscosity and density, μ^* and ρ^*.

The modified Eckert's reference temperature method is used from Ref. 11 to estimate the boundary layer properties defined by a temperature somewhere in the boundary layer T^*

$$T^* = T_e\left(0.45 + 0.55\frac{T_w}{T_e} + 0.16r\frac{\gamma - 1}{2}M_e^2\right) \tag{5}$$

where for laminar flow the recovery factor, r, is $r = \sqrt{Pr}$ and for turbulent flow $r = Pr^{1/3}$, where Pr is the Prandtl number. The variables with the w subscript refer to the wall properties whereas those with e refer to the boundary layer edge. The reference viscosity and density are then recomputed from the reference temperature using the Sutherland's formula and the ideal gas law.

C. Computation of Metric Coefficients

Calculation of the heat-transfer rate and the skin-friction drag using the method of an axisymmetric analogue has been in use by NASA ever since it was first formulated by Cooke in 1961.[2] The axisymmetric geometry is translated into 3D using the so-called metric coefficient, h, which expresses the rate of divergence of the streamlines and would be equivalent to the body radius at a given x-coordinate in case of an axisymmetric configuration. It is this metric coefficient, which requires a rather accurate representation of the inviscid velocity field, so that this divergence of streamlines can be estimated.

The computation of the metric coefficient can be done using several techniques such as the ones suggested by Hamilton[7] and by Parzhikar.[8] In case of the former, following the reasoning of Hamilton, the surface can be fitted using the following quadratic formula assuming x to be the dependent coordinate:

$$y_1^2 a_1 + y_1 a_2 + z_1^2 a_3 + z_1 a_4 + x_1^2 a_5 + x_1 a_6 + a_7 = 0 \tag{6}$$

from which it can be seen that assuming six equations, a_7 is a free variable. It can be set to 1 for majority of the elements as done in the original reference,[7] apart from when $x = y = z = 0$, which requires that $a_7 = 0$. In addition, from the analysis of unit vectors in the direction of the streamline and normal it follows that

$$uF_x + vF_y + wF_z = 0 \rightarrow$$

$$2v_1y_1a_1 + v_1a_2 + 2w_1z_1a_3 + w_1a_4 + 2u_1x_1a_5 + u_1a_6 = 0 \tag{7}$$

These two quadratic formulae are applied to all vertices of an element,

$$a_1 + y_2a_2 + z_2^2a_3 + z_2a_4 + x_2^2a_5 + x_2a_6 + a_7 = 0$$

$$2v_2y_2a_1 + v_2a_2 + 2w_2z_2a_3 + w_2a_4 + 2u_2x_2a_5 + u_2a_6 = 0$$

...

such that a system of six equations and six unknowns is obtained. After inversion, the coefficients a_1 through a_6 are obtained, and the velocity derivatives necessary for computation of the metric are determined.

Then, during the downstream marching, the determination of the metric coefficient (beyond the stagnation region) is done using the velocity derivative data according to the following rule:

$$h = w\left(\frac{\partial y}{\partial z}\right)_z \frac{|\nabla \mathbf{F}|}{F_x V} \tag{8}$$

in which F_x and $\nabla\mathbf{F}$ follow from the quadratic surface fitting functions found with a_1 to a_6 as

$$F_x = 2a_5x + a_6 \qquad F_y = 2a_1y + a_2 \qquad F_z = 2a_3z + a_4 \tag{9}$$

$$\nabla \mathbf{F} = \sqrt{F_x^2 + F_y^2 + F_z^2}. \tag{10}$$

Afterwards, during the downstream marching, the $w\left(\frac{\partial y}{\partial z}\right)_z$ is integrated along the way from the stagnation point as

$$\frac{\mathrm{D}}{\mathrm{D}s}\left[w\left(\frac{\partial y}{\partial z}\right)_z\right] = \frac{w}{V}\left(\frac{\partial y}{\partial z}\right)_z\left(\frac{\partial w}{\partial y} + \frac{\partial w}{\partial z}\right) \tag{11}$$

On the other hand, in the method of Perzhikar,[8] the velocity derivatives and surface fits are not necessary. The method relies on the fact that two neighbouring streamlines can be found emanating from a close neighbourhood at the stagnation line, and their distance at each point can represent this divergence, which can be determined directly by perpendicular projection. The parameter hd_β is defined for this purpose, which is the perpendicular distance between these two neighbouring streamlines given by

$$hd_\beta = h_\beta d_\beta \sin\gamma \tag{12}$$

Here, $h_\beta d_\beta$ is the distance between two points p_n and p_i on the two streamlines having the same surface distance to the stagnation region. In this context, γ is then the angle that exists between the $p_n \rightarrow p_i$ line and the rest of the original streamline along which the metric coefficient is evaluated, which can be represented by for example taking p_{i-1}. The cosine rule can then be used to compute γ as

$$|\mathbf{x}(p_n - p_{i-1})|^2 = |\mathbf{x}(p_n - p_i)|^2 + |\mathbf{x}(p_i - p_{i-1})|^2 - 2|\mathbf{x}(p_n - p_i)||\mathbf{x}(p_i - p_{i-1})|\cos\gamma \tag{13}$$

Both approaches were analysed in the scope of the work and assessed in their reliability given the fairly inaccurate representation of the velocity field from the Newtonian technique.

D. Determination of Heat Flux, Boundary-Layer Growth and Skin-Friction Coefficient

Having determined the metric coefficient, the approximate axisymmetric relations can be used to estimate the boundary-layer growth, heat-transfer rate and the skin-friction coefficient. The integration is carried downstream from the streamlines, which were back-traced from each node down to the stagnation region. First, the stagnation-point heating is determined according to Ref. 12 as

$$q_{w_s} = 0.767(\rho\mu)_{e,s}^{0.43}(\rho\mu)_{w,s}^{0.07}\left(\frac{\mathrm{d}u}{\mathrm{d}S}\right)_{e,s}^{0.5}(H_s - H_w)(Pr)^{-0.6} \tag{14}$$

where the subscripts e, s refer to stagnation point edge properties and w, s to stagnation point wall properties. The term $\left(\frac{\mathrm{d}u}{\mathrm{d}S}\right)_{e,s}$ can be approximated as

$$\left(\frac{\mathrm{d}u}{\mathrm{d}S}\right)_{e,s} \approx \frac{1}{\epsilon}\sqrt{2\frac{p_e - p_\infty}{\rho_w}} \tag{15}$$

The boundary layer momentum thickness integral in the stagnation region is evaluated as[7]

$$\int_0^s \rho^* u_e \mu^* h^2 \mathrm{d}s = (\rho^*\mu^*)_s u_{e,\epsilon} h_\epsilon^2 \frac{\Delta s}{4} \tag{16}$$

where the viscosity and density are evaluated at the stagnation point. The ϵ line represents the the line around the stagnation point defining the stagnation region, from which tracing of the streamlines starts. The metric coefficient and the velocity in Eq. (16) are evaluated at this ϵ line. After the crossing of the stagnation line, a laminar regime is assumed at first.

In laminar flow, according to the original method of Cooke,[2] the boundary-layer momentum thickness, θ_L, can be estimated as

$$\theta_L = 0.664\frac{\left(\int_0^s \rho^*\mu_e\mu^* h^2 \mathrm{d}s\right)^{0.5}}{\rho_e u_e h} \tag{17}$$

where the trapezoid rule is used for integration. Note that in Eq. (17), h refers to the local metric coefficient. Finally, to determine the heat flux, the edge enthalpy, the wall enthalpy and the adiabatic enthalpy must be defined,

$$H_e = c_p T_e \qquad H_w = c_p T_w \qquad H_{aw} = H_e + r\frac{V_e^2}{2} \tag{18}$$

and, with the boundary-layer-momentum-thickness-based Reynolds number, $Re_{\theta,e}$, given by

$$Re_{\theta,e} = \frac{\theta_L V_e \rho_e}{\mu_e} \tag{19}$$

Finally, the heat flux $\dot{q}_{w,L}$ can then be approximated with

$$\dot{q}_{w,L} = 0.22\frac{1}{R_{\theta,e}}\frac{\rho^*}{\rho_e}\frac{\mu^*}{\mu_e}\rho_e u_e (H_{aw} - H_w) Pr_w^{-0.6} \tag{20}$$

The skin friction coefficient C_f then has the form of

$$C_f = \frac{2\dot{q}_{w,L} Pr^{2/3}}{\rho_e u_e c_p (T_{aw} - T_w)} = \frac{2\dot{q}_{w,L} Pr^{2/3}}{\rho_e u_e (H_{aw} - H_w)} \tag{21}$$

It is apparent that as the momentum thickness grows downstream, due to its inverse proportionality in the form of $Re_{\theta,e}$, the heat flux will decrease downstream, as expected.

At some point downstream, the heat flux will rise again due to the transition of the flow. The transition to turbulence was based on the evaluation of two transition criteria,[9]

$$Re_T = 6.421\mathrm{e}^{1.209\cdot 10^{-4} M_e^{2.641}} \tag{22}$$

and

$$\frac{Re_{\theta_T}}{M_e} = 100 \tag{23}$$

where the former one has been in use for the analysis of waveriders, whereas the latter one was used while designing the Space Shuttle.

In the turbulent regime, in a form similar to the laminar momentum-boundary-layer thickness, θ_T, can be approximated as[2]

$$\theta_T = \frac{\left(c_2 \int_0^s {\mu^*}^m \rho^* U_e h^{c_3} \mathrm{d}s\right)^{c_4}}{\rho_e U_e h} \tag{24}$$

with the following expressions for the constants c_1 to c_5:

$$c_5 = 2.2433 + 0.93N \quad c_3 = 1 + m \quad c_4 = \frac{1}{c_3} \quad c_2 = (1+m)c_1 \quad c_1 = \frac{c_5^{-2N/(N+1)}}{\left[\frac{N}{(N+1)(N+2)}\right]^{-m}} \tag{25}$$

The variable N can be expressed as a function of the momentum-thickness-based Reynolds number from the data gathered in Ref. 13,

$$N = 12.67 - 6.5 \log R_{\theta_e} + 1.21 \log^2 R_{\theta_e} \tag{26}$$

The integration on θ_T is based on the same principle as in the laminar flow, according to

$$\theta_T = \frac{\left(c_2 \int_0^s {\mu^*}^m \rho^* U_e h^{c_3} \mathrm{d}s\right)^{c_4}}{\rho_e U_e h} \tag{27}$$

where again, the trapezoid rule is used for integration. With the known momentum thickness, the heat flux is determined by

$$\dot{q}_{w_T} = c_1 \frac{1}{Re_{\theta_e}^m} \left(\frac{\mu^*}{\mu_e}\right)^m \frac{\rho^*}{\rho_e} \rho_e U_e (H_{aw} - H_w)(Pr)^{-0.4} \tag{28}$$

Finally, the skin friction is found via

$$C_f = 2c_1 \left(\frac{1}{Re_{\theta,e}^m}\right) \tag{29}$$

These expressions are evaluated at each step of each streamline until the original node location is reached, from which the streamline originally emanated. The final values at the end of the streamline are then representative of the heat flux and skin friction at that node.

III. Numerical Implementation

The numerical execution is three-fold. First, the code uses the modified Newtonian technique to estimate the inviscid flow field and projects the velocity onto the vehicle surface for determination of the velocity vector. This can be only evaluated on the cell-centred basis. Thus, afterwards, the inverse distance weighting is used for node interpolation of the inviscid flow field.

Afterwards, the streamlines originating from each mesh node are back-traced down to the stagnation region, which is defined by the ϵ-curve. For the cases discussed in this paper, the ϵ curve is circular. The method has been also developed for cases of multiple stagnation regions, but since the exact shock shape and its interaction with the boundary layers of geometries, which might extend beyond it cannot be determined from the simple Newtonian technique, this application still requires further development.

Due to the relatively large inaccuracies in the velocity field, especially for more complex geometries, it was found that the use of Hamilton's method to determine the metric coefficient, required for the use of the axisymmetric analogue, was oftentimes numerically unstable. Therefore, the method of Parzhikar is used to determine the metric coefficient.

The Parzhikar method requires the point p_{i-1} at the streamline (see Eq. (13)). Since this point is not available at the end of the streamline at the original node, the streamline is linearly extrapolated at that point to allow for the determination of the local metric coefficient. To choose which reference streamline to use when computing the metric coefficient, a function considering the distance of the initial starting points of the two streamlines and also of the final points of the streamlines is used. This is to avoid selection of a reference streamline which could potentially lead to another stagnation region or a leading edge.

Finally, the downstream marching following the back-traced streamlines from the stagnation region, allowing for step-wise integration of the momentum thickness boundary layer, determines the local heat flux

and skin friction at each node on the windward side of the vehicle. The flow initially starts as laminar, and once either of the criteria defined in Eqs. (22) and (23) becomes satisfied, the flow is further considered as turbulent. The onset of transition can also be prescribed by the user, either in terms of x or Re_x. Once the viscous calculations are finished, the lift and drag coefficients can be re-computed taking the friction coefficient into account.

IV. Validation Results

A. Testcases

To evaluate the errors due to the use of the modified Newtonian method, seven different cases were evaluated. The summary of the cases, along with the references to the original data, is shown in Table 1.

The cases were selected to represent various free-stream conditions over which the accuracy of the modified Newtonian technique changes (ranging from Mach 6 to Mach 12.9), since the modified Newtonian technique is known to become more accurate as the free-stream Mach number increases.[9] In addition, various scales (from 0.008 scale of the Space Shuttle to the full scale) and various geometries, with a simple blunted cone geometry and a complex geometry of the Space Shuttle, were also included.

Figures 2 through 12 show the match between the applied technique, the axisymmetric analogue method by Hamilton, when Euler solutions are used, and experimental data, when available.

Since the present technique scales proportionally with the number of cells used, and since the purpose of this technique is to increase the speed of initial stages of optimisation studies, a relatively coarse mesh was selected for the cases presented. For cases 1, and 4 through 6, 12,000 vertices were used in the mesh. For case 3, to evaluate the effects of discretisation, 50,000 vertices were used. Finally, for case 7, due to the simple blunted cone geometry, only a 2,500-vertex mesh was generated.

Table 1. The validation cases used to evaluate the errors of using the developed technique.

	Study	Mesh	Scale	α [°]	M_∞	T_∞ [K]	p_∞ [Pa]	ρ_∞ [$\frac{kg}{m^3}$]	μ_∞ [$\frac{kg}{ms}$]
1	Hamilton (2009)[7]	Space Shuttle	Full	40	12.9	261.6	40.0	5.33e-4	1.72e-5
2	Hamilton (2009)[7]	Space Shuttle	0.008	25	6.0	62.87	580.0	3.13e-2	4.20e-6
3	Hamilton (1987)[4]	Space Shuttle	0.0175	35	7.92	52.5	159.0	1.06e-2	3.38e-6
4	Hamilton (1987)[4]	Space Shuttle	Full	35	9.15	260.0	100.0	1.34e-3	1.65e-5
5	DeJarnette (1985)[5]	Space Shuttle	0.0175	35	8.0	54.0	607.0	3.92e-2	4.40e-7
6	Hamilton (2009)[7]	Blunted Cone	Full	20	6.0	62.87	580.0	3.13e-2	4.20e-6
7	Hamilton (2009)[7]	Blunted Cone	Full	20	6.0	62.87	580.0	3.13e-2	4.20e-6

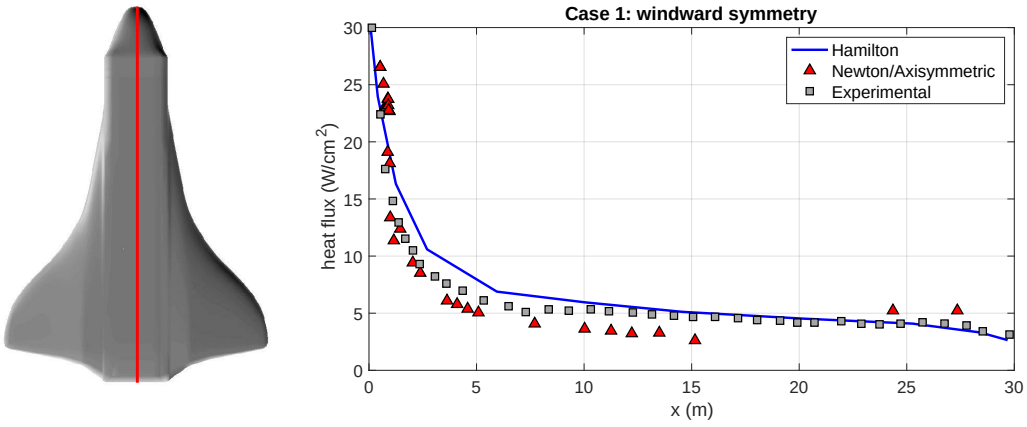

Figure 2. Comparison between the experimental data, Euler/ axisymmetric approach and the technique applied in this work for Case 1 from Table 1. Shown is the windward symmetry plane.

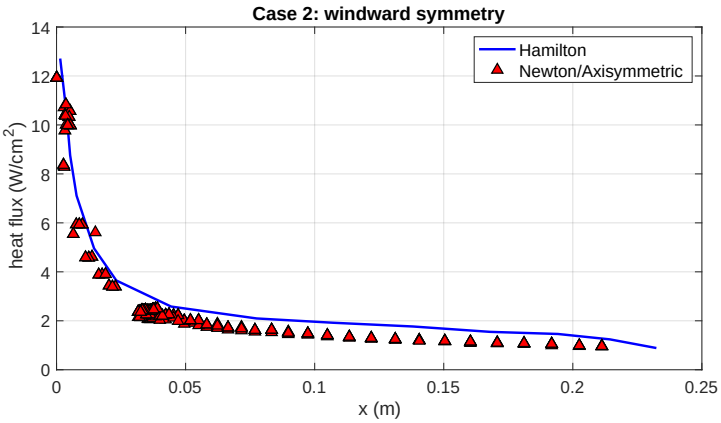

Figure 3. Comparison between the experimental data, Euler/ axisymmetric approach and the technique applied in this work for Case 2 from Table 1. Shown is the windward symmetry plane.

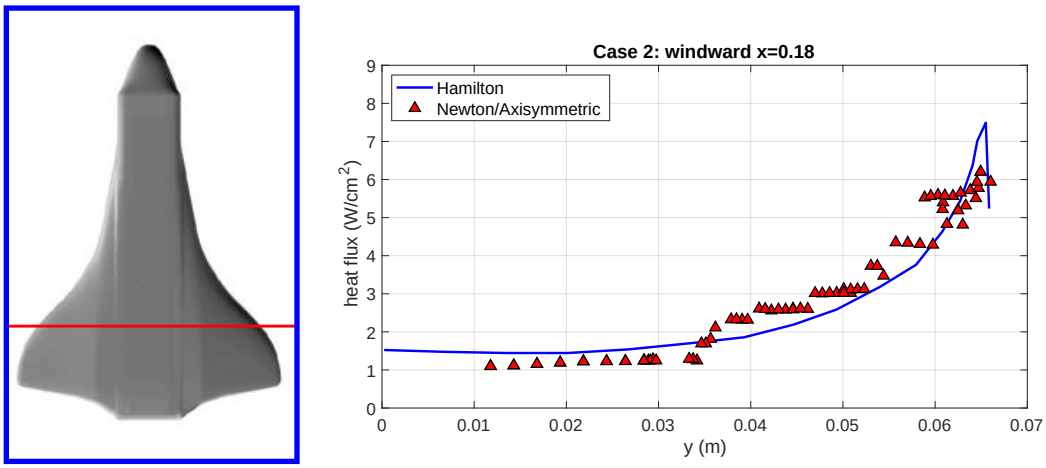

Figure 4. Comparison between the Euler/ axisymmetric approach and the technique applied in this work for Case 2 from Table 1. Shown is the y-plane at $x = 0.18$ m.

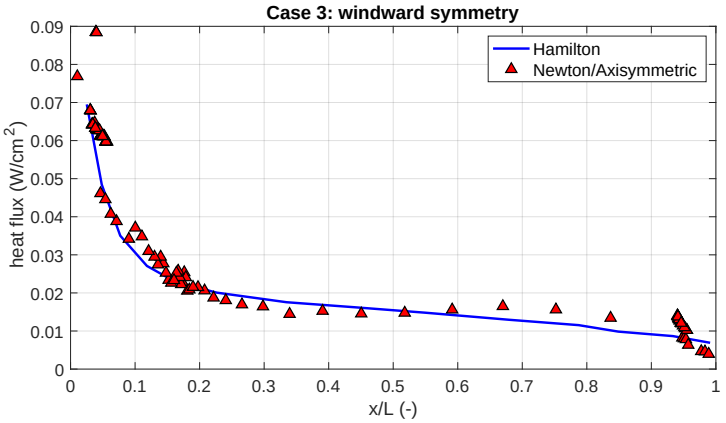

Figure 5. Comparison between Euler/ axisymmetric approach and the technique applied in this work for Case 3 from Table 1. Shown is the windward symmetry plane.

It can be seen that in general, the trends are well represented with the errors on average below 20-30%. However, locally, the errors can become very large, which is usually due to inaccurate resolution of

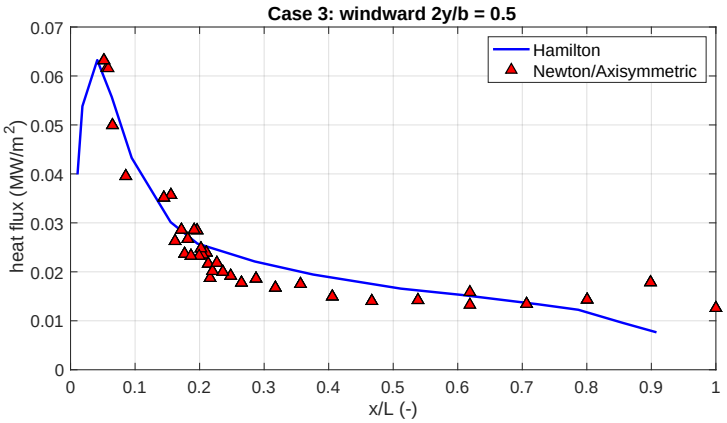

Figure 6. Comparison between the Euler/ axisymmetric approach and the technique applied in this work for Case 3 from Table 1. Shown is the y plane at $x = 0.18$ m.

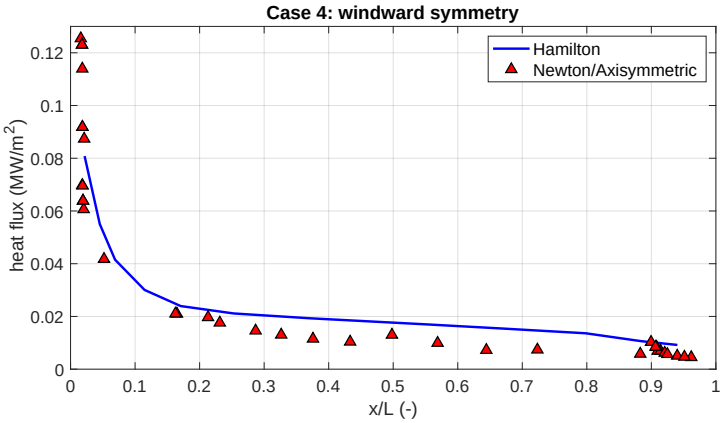

Figure 7. Comparison between the Euler/ axisymmetric approach and the technique applied in this work for Case 4 from Table 1. Shown is the windward symmetry plane.

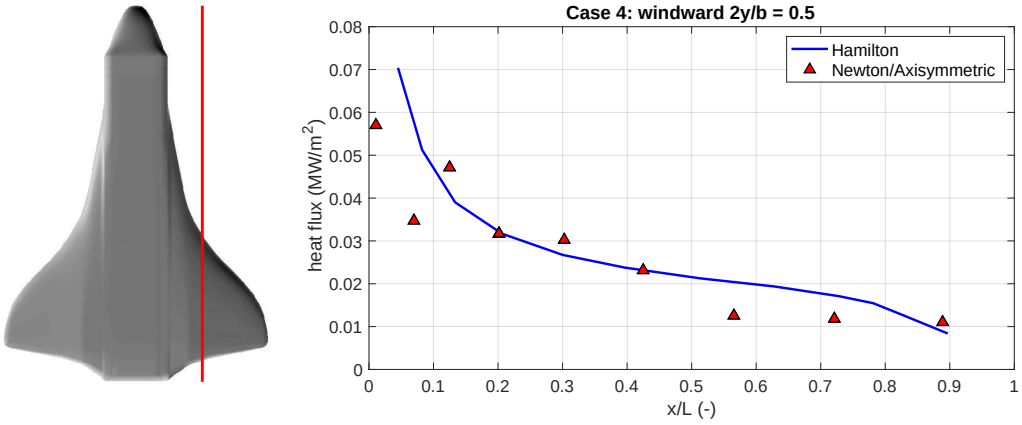

Figure 8. Comparison between the Euler/ axisymmetric approach and the technique applied in this work for Case 4 from Table 1. Shown is the x-plane at $y = b/4$ for laminar flow.

the metric coefficient. This comes from the fact that the velocity field necessary to recreate the surface streamlines comes from a simple projection onto the surface, allowing the computed streamlines to cross in

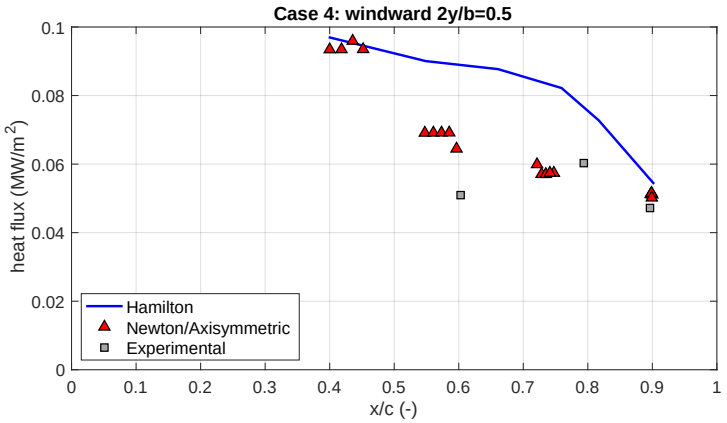

Figure 9. Comparison between the Euler/ axisymmetric approach and the technique applied in this work for Case 4 from Table 1. Shown is the x-plane at $y = b/4$ for turbulent flow.

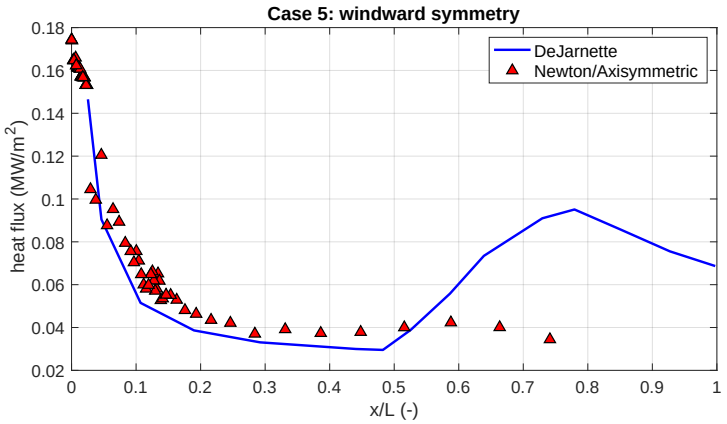

Figure 10. Comparison between the Euler/ axisymmetric approach and the technique applied in this work for Case 5 from Table 1. Shown is the windward symmetry plane.

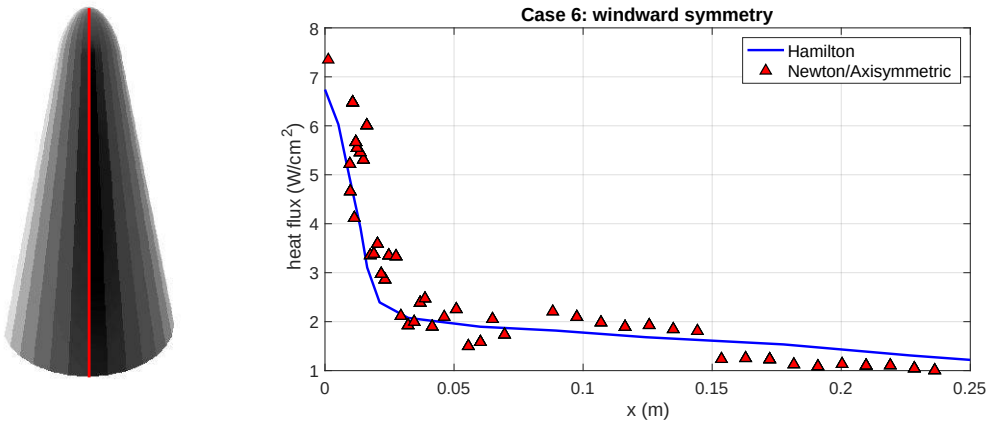

Figure 11. Comparison between the Euler/ axisymmetric approach and the technique applied in this work for Case 6 from Table 1. Shown is the windward symmetry plane for laminar flow.

more geometrically complex regions. The distance between two neighbouring streamlines is used to compute the metric coefficient, which directly enters the calculation of heat flux and momentum-boundary-layer

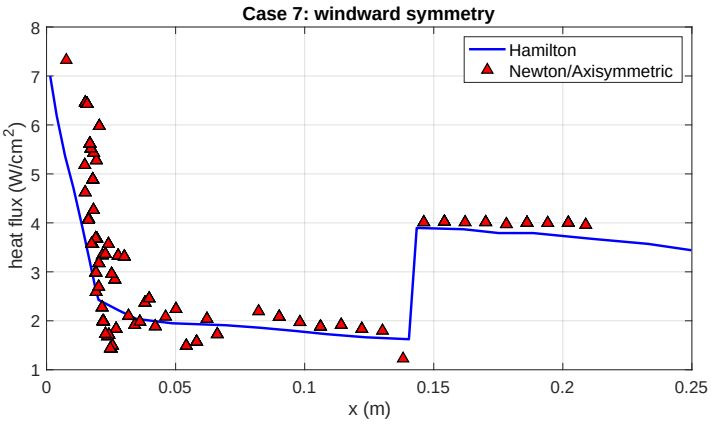

Figure 12. Comparison between the Euler/ axisymmetric approach and the technique applied in this work for Case 7 from Table 1. Shown is the windward symmetry plane for tripped flow.

thickness, as seen in Eqs. (17), (20), (24) and (28). Thus, any error in the resolved velocity field translates into an error in the estimated heat flux. As a result, also many erroneous nodes, with a very low reported heat flux, can be present in the solution and ideally should be re-traced with different numerical settings.

Larger errors can also be seen for the turbulent heat flux over the Space Shuttle wing in Fig. 9. Since the initial heat flux at 0.4 x/c matches very well, these offsets are at least partly caused by the inaccuracies in the geometry of the Space Shuttle mesh, since the exact geometry used in the validation study could not be reproduced. Curiously however, the supposedly inaccurate Newtonian-technique-based data seems to be in a better agreement with the experimental (flight) data compared to the results from an Euler solution.

B. Computational Performance

The speed of the solver is of essence, since it was developed solely with the purpose of rapid approximation of aerodynamics. The programme was written in Python, but is intended to be translated to Fortran for speed reasons. The time required for completion of various modules of the code for three different discretisation levels is shown in Table 2. The speed was measured on a personal computer (Macbook Air 2018, 1,6 GHz Intel Core i5 processor, 8GB of two 2,133MHz LPDDR3 RAM, OS X version 10.14).

From Table 2, it is clear that the back-tracing and metric computation modules dictate the overall performance limits of the solver. This is mostly due to the use of unstructured meshes, where for each point on each streamline, the local nearest cell must be found to approximate the velocity field. This has already been partially improved by artificial partitioning of the geometry into various sub-entities, but further work is recommended to decrease the computational time. Obviously, significant improvement in speed can also be achieved with parallelisation of the code. Now, with the numerical methods and the performance discussed, the solver can be applied to a shape-optimisation study.

Table 2. Approximate time required for calculations of varying complexity

		Average time of computation [s]		
Problem size		Large (50,000)	Medium (12,000)	Small (2,500)
Mesh Processor		0.5 - 0.7	0.25 - 0.35	0.08 - 0.12
Inviscid Solver		0.5 - 0.7	0.25 - 0.35	0.08 - 0.12
Viscous solver				
	Back-tracing	500 - 600	120 - 150	30 - 40
	Metric computation	500 - 600	120 - 150	30 - 40
	Marchdown	14 - 18	3.5 - 4.5	0.8 - 1.2

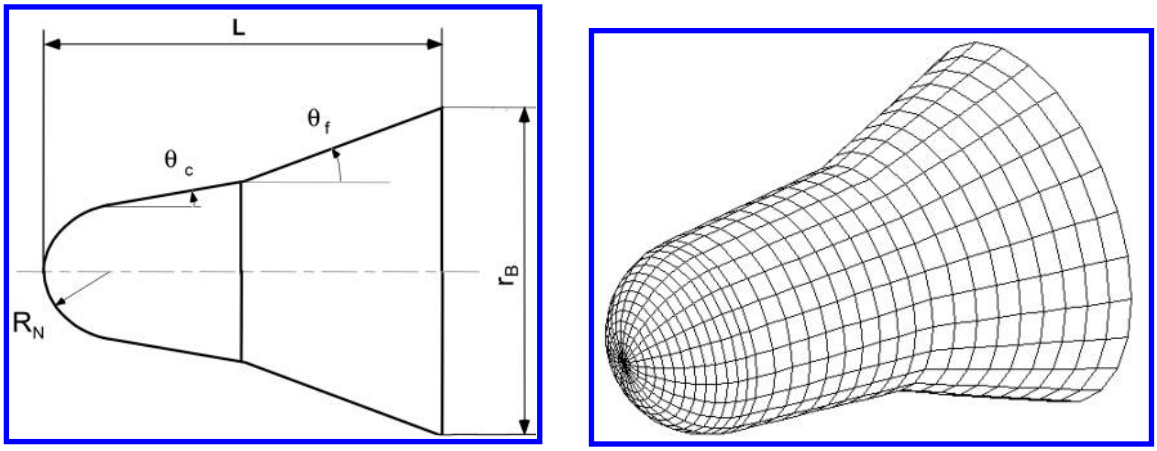

(a) Geometry (b) Nominal configuration

Figure 13. The bi-conic re-entry capsule.

V. Shape-Optimisation Application

A. Setup

The optimisation study on which the developed technique will be applied is similar to the one presented for the biconic vehicle DART by Sudmeijer and Mooij in 2002.[1] DART was designed for in-flight aerodynamic experiments with strong Shock-Wave Boundary-Layer interaction, but as a result there would be high thermal fluxes on the flare. The shape optimisation study was meant to give more insight in the relation between the geometrical parameters and the heat flux in the nose, and on the cone and flare.

The biconic shape was chosen for its simplicity, as it can easily be described by a limited number of geometrical parameters. The outer geometry of the (biconic) re-entry capsule is fully determined by five parameters (Fig. 13(a)): the nose radius, R_N, the semi cone-angle, θ_c, the semi flare-angle, θ_f, the vehicle length, L, and the base radius, r_B. The maximum vehicle length shall not be more than 1.6 m, because of the available space inside the fairing of the selected launcher (the submarine-launched VOLNA, a former Russian ICBM). The nominal configuration was set at $R_N = 0.3$ m, $\theta_c = 5°$, $\theta_f = 20°$, $L = 1.45$ m, and $r_B = 0.6$ m; the corresponding vehicle mesh is shown in Fig. 13(b).

The optimisation methodology was as follows. A discrete number of shape variations was defined to limit the potentially large number of evaluations. These variations were determined with techniques from the world of design of experiments, and the selected design was the so-called central composite design (CCD). In CCD, a subset of the configurations is based on a (fractional) factorial design, then per design parameter two extreme points (the so-called axial points) are defined, and one (or more) centre point(s) (*i.e.,* the nominal configuration) is (are) chosen. For five design parameters, a minimum of 27 configurations is required to be evaluated. Subsequent steps would then be to set up response surfaces for selected objectives after the evaluation of each configuration, optimise these surfaces rather than directly optimising the shapes, and only do a verification evaluation for the found optimum. Each evaluation would involve the generation of a vehicle surface mesh, an aerodynamic evaluation, a simulation of the ballistic trajectory, and the evaluation of several objectives along this trajectory, amongst others, the heat flux at the three locations and the maximum *g-load*. Initial conditions at $h = 120$ km for this ballistic trajectory are a velocity of $V_0 = 5{,}250$ m/s, a flight-path angle of $\gamma_0 = -6.5°$, whereas the longitude and latitude are arbitrarily zero-initialised. The entry flight is along the equatior in eastward direction, so the heading is $\chi_0 = 90°$. Finally, the vehicle mass is constant for all configurations, *i.e.,* $m = 200$ kg.

In the current paper we are mainly interested in the effect that using the proposed aerothermodynamics modelling will have on the fluxes, as compared to those found earlier.[1] Therefore, we will evaluate only the input set of 27 configurations, which have been listed in Table 3[a]. The fractional factorial portion of

[a]It is noted that in the original study, two sets of analyses were done, one with a variation of all five parameters, and one with only four, having fronzen the base radius. Reason for the second analysis was that for the former, the variation of the fluxes was too non-linear to capture that in a response surface. In the current paper we stick to the original set of configurations, even though the fifth configuration led to an infeasible geometry. But, with the remaining 26 configurations, sufficient geometry

Table 3. Central Composite Design of bi-conic re-entry capsule.

	Design	R_N (m)	θ_c (°)	θ_f (°)	L (m)	r_B (m)
1	L16 row #01	0.235	1.767	16.767	1.353	0.568
2	L16 row #02	0.235	1.767	16.767	1.547	0.632
3	L16 row #03	0.235	1.767	23.233	1.353	0.632
4	L16 row #04	0.235	1.767	23.233	1.547	0.568
5	L16 row #05	0.235	8.233	16.767	1.353	0.632
6	L16 row #06	0.235	8.233	16.767	1.547	0.568
7	L16 row #07	0.235	8.233	23.233	1.353	0.568
8	L16 row #08	0.235	8.233	23.233	1.547	0.632
9	L16 row #09	0.365	1.767	16.767	1.353	0.632
10	L16 row #10	0.365	1.767	16.767	1.547	0.568
11	L16 row #11	0.365	1.767	23.233	1.353	0.568
12	L16 row #12	0.365	1.767	23.233	1.547	0.632
13	L16 row #13	0.365	8.233	16.767	1.353	0.568
14	L16 row #14	0.365	8.233	16.767	1.547	0.632
15	L16 row #15	0.365	8.233	23.233	1.353	0.632
16	L16 row #16	0.365	8.233	23.233	1.547	0.568
17	-Axial #01	0.200	5.000	20.000	1.450	0.6000
18	Axial #01	0.400	5.000	20.000	1.450	0.6000
19	-Axial #02	0.300	0.000	20.000	1.450	0.6000
20	Axial #02	0.300	10.000	20.000	1.450	0.6000
21	-Axial #03	0.300	5.000	15.000	1.450	0.6000
22	Axial #03	0.300	5.000	25.000	1.450	0.6000
23	-Axial #04	0.300	5.000	20.000	1.300	0.6000
24	Axial #04	0.300	5.000	20.000	1.600	0.6000
25	-Axial #05	0.300	5.000	15.000	1.450	0.550
26	Axial #05	0.300	5.000	25.000	1.450	0.650
27	centre point	0.300	5.000	20.000	1.450	0.600

the design follows from a so-called L_{16} orthogonal array to define the geometry-parameter combinations. Matrix orthogonality, in this context, should be considered in the combinatorial sense, namely: for any pair of columns in the matrix, all combinations of parameter (or factor) levels occur an equal number of times, the so-called balancing property.[14]

In the original study by Sudmeijer and Mooij, the modified Newtonian method was used to resolve the inviscid field. However, since skin friction was not computed, the (ballistic) trajectory was only determined from the inviscid pressure forces and moments. In addition, semi-empirical formulas to estimate the maximum heat flux over the cone and the flare portions of the vehicle were used; for the sake of completeness, this will be discussed in the next sub-section, Sec. V.B. These semi-empirical formulas assumed laminar flow over the nose and the cone, flow transition located at the interface between the cone and the flare and turbulent flow over the flared part of the geometry. To evaluate the fluxes with the new model proposed in this paper, we will use the same ballistic trajectory; justification for this will be given in Sec. V.C.

B. Simplified Heat-Flux Model

The heat flux on the nose, the cone and the flare for the complete re-entry flight are determined by engineering approximations based on existing literature.[9,15] For both stagnation-point flux and cone flux a laminar flow is assumed, whereas for the flare flux a turbulent flow is assumed, with the transition point in the cone-flare junction. The heat flux in the stagnation point on the nose can be estimated by the classical Chapman relation for a wall temperature of 300 K, the so-called cold-wall model

variation is captured, including the one of the base radius. For more details about the optimisation methodology, as well as the field of design of experiments, the reader is referred to the original study and the references therein.

$$q_{c_{300}} = \frac{C}{\sqrt{R_N}}\sqrt{\frac{\rho_\infty}{\rho_0}}\left(\frac{V_\infty}{V_c}\right)^3 \tag{30}$$

with $C = 1.06584 \cdot 10^8 W\sqrt{\text{m}}$ and $V_c = 7,905$ m/s. The stagnation heat flux corrected for the actual outer wall temperature, to be calculated from radiation equilibrium, is

$$q_c(t) = \frac{q_{c_{300}}(t)}{T_{aw}(t) - 300}[T_{aw}(t) - T_w(t)] \tag{31}$$

In the above equation, the adiabatic wall temperature T_{aw} is calculated with

$$T_{aw}(t) = T_\infty + r\frac{V_\infty^2}{2c_p} \tag{32}$$

with T_∞ and V_∞ being the free-stream temperature and velocity, respectively, r is the recovery factor ($r = 1$ for a laminar flow), and c_p is the specific heat coefficient at constant pressure.

The heat flux on the cone is determined by

$$q_{c,cone} = St\rho_e V_\infty \cos\theta_c c_p[T_{aw}(t) - T_w(t)]\sqrt{3} \tag{33}$$

In this equation, which has originally been defined for a wedge with wedge angle θ_c, the constant $\sqrt{3}$ corrects for the flow being three dimensional. The Stanton number St follows from

$$St = \frac{0.332}{\sqrt{Re_x^*}}(Pr^*)^{\frac{2}{3}} \tag{34}$$

The asterix of the Reynolds and Prandtl numbers refers to the evaluation of these numbers at the reference temperature, defined by:

$$T_e* = 0.28\,T_e + 0.5\,T_w + 0.22\,T_{aw} \tag{35}$$

with the temperature at the edge of the boundary layer, T_e, given by

$$T_e = T_\infty\left[\frac{2\gamma(\gamma-1)}{(\gamma+1)^2}\right]M_\infty^2\sin^2\beta \tag{36}$$

and the shock angle, β, follows from shock-wave theory, where its assumed that the streamlines at the edge of the boundary layer passed an oblique shock wave:

$$\beta = \frac{\theta_c F(M_\infty)}{M_\infty^2} + \sqrt{\left(\frac{\theta_c F(M_\infty)}{M_\infty^2}\right)^2 + \frac{1}{M_\infty^2}} \tag{37}$$

with

$$F(M_\infty) = (\gamma+1)M_\infty^2 + 2 \tag{38}$$

Note that Eq. (37) is valid for a two-dimensional wedge flow. However, the shock angle of a cone is smaller than for a wedge, but the shock of a blunted cone is curved and as a result higher shock angles are expected. Also the Reynolds number at the edge of the boundary layer is influenced considerably by the entropy layer caused by the blunt nose that reduces the velocities at the edge of the boundary layer. The Reynolds numbers are corrected for this entropy effect by a method based on measurements, as proposed by Krasnov.[15]

The heat flux on the flare can be estimated by

$$q_{c,flare}(z) = c_p\rho_f v_f\,(T_{aw} - T_f)\,A\left(\frac{T_f}{T_f^*}\right)^{1-2n}\left(\frac{T_f\mu^*}{T_f^*\mu_f}\right)^n\left(\frac{\mu_f}{\rho_f v_f z}\right)^n \tag{39}$$

where z is the length of the boundary layer over the flare along a meridian.[16] The boundary layer of the flare past the shock wave of the cone-flare junction is assumed to be turbulent, so in Eq. (39) the values $n = 0.2$ and $A = 0.575$ can be used. T_f and μ_f are the temperature and the viscosity at the edge of the

boundary layer of the flare, respectively, and T_f^* is the reference temperature at the flare, evaluated with Eq. (35). The temperature on the flare can be calculated by

$$T_f = T_\infty \left(1 + \frac{\gamma - 1}{2} M_\infty \sin^2\theta_f\right) \left\{1 + \left[\frac{T_e}{T_\infty} - 1\right] \left[1 - e^{c\left(\frac{z}{\delta_{bl}}+1\right)}\right]\right\} \tag{40}$$

with c = -0.412.

The viscosity at the edge of the boundary layer of the flare is obtained with Sutherland's equation,

$$\mu_f = \frac{B_\mu T_f^{\frac{3}{2}}}{T_f + S_\mu} \tag{41}$$

where $B_\mu = 1.458{\cdot}10^{-6}$ Pa s K$^{-1/2}$ is a constant depending on the gas and $S_\mu = 110.4$ K is Sutherland's constant. Finally, the boundary-layer thickness of the cone near the cone-flare junction is given by

$$\delta_{bl} = \frac{5 L_c}{\cos\theta_c \sqrt{\mathrm{Re}_{L_{lam}}}} \tag{42}$$

A correction of the specific heat for high temperature effects is applied with[15]

$$c_p = c_{p_\infty} \left(\frac{T}{T_\infty}\right)^{0.1} \tag{43}$$

C. Influence of Skin Friction on the Trajectory

As mentioned above, the trajectory computation in the original optimisation study was based purely on the inviscid calculations with the Newtonian technique. In the present calculation, the skin friction coefficient on the windward side can also be resolved. It should be noted that for some geometries where the leeward side could heavily contribute to the viscous forces, the results presented below might not apply. Correcting for this limitation this is left for future code development.

The skin-friction coefficient was computed at the original trajectory points and the total inviscid and viscous forces added to recompute the total drag coefficient. It is found that for the portion of the flight where aerodynamic forces become dominant and relevant for design optimisation, the inviscid forces are far more significant than the viscous forces. An example of this is shown in Fig. 14, where the effect of using either the inviscid drag coefficient or the one including the viscous forces is shown for the nominal vehicle configuration. These two simulations have been done with a simplified model, derived for a non-rotating spherical Earth, which is in this case allowed, as we are aiming for a *relative* comparison. For each time step of $\Delta t = 1$ s with the Runge-Kutta fourth-order integrator, an average value of C_D for that interval is used. This way of simulation was the simplest way to do the comparison, as normally the coefficient would be dependent on Mach number, altitude, and wall temperature, and an iterative procedure would be required to obtain the trajectory.

What can be seen in the figure is that in the initial flight phase C_D is more than four times as large due to the viscous contribution. However, because the dynamic pressure is very small, the drag force is equally small. The difference in drag is therefore negligible and the trajectories, simulating for either case, are overlapping, as can be seen in the altitude-velocity diagram. Therefore, also the stagnation-point heat flux – calculated with the simple cold-wall Chapman model for laminar flow – and the *g-load* profiles are overlapping.

What can be concluded from this is that the trajectories used in the original study,[1] and obtained using the inviscid (modified Newtonian) drag coefficient, can also be used in the current paper. It also means that this study can now mainly focus on the effects of the updated heat-flux results on the choice of the optimal configuration, and factors such as *g-load* do not have to be re-visited.

D. Recalculation of the Heat Fluxes and the Transition Problem

The maximum heat fluxes were computed for each part of the geometry (stagnation region, the cone and the flare) at each point of the trajectory with the present method and compared with the original study.

The results for the maximum stagnation point heat flux match well with the original data, with offsets within 20% as is indicated in Fig. 15. This is expected since the semi-empirical methods available for

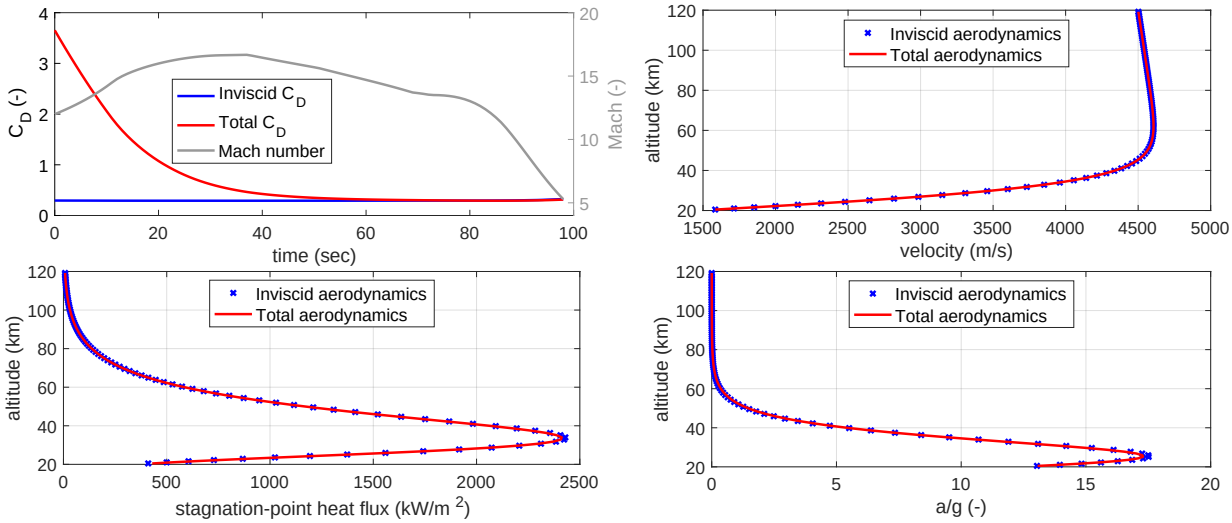

Figure 14. Effect of difference in drag coefficient on the trajectory and associated parameters.

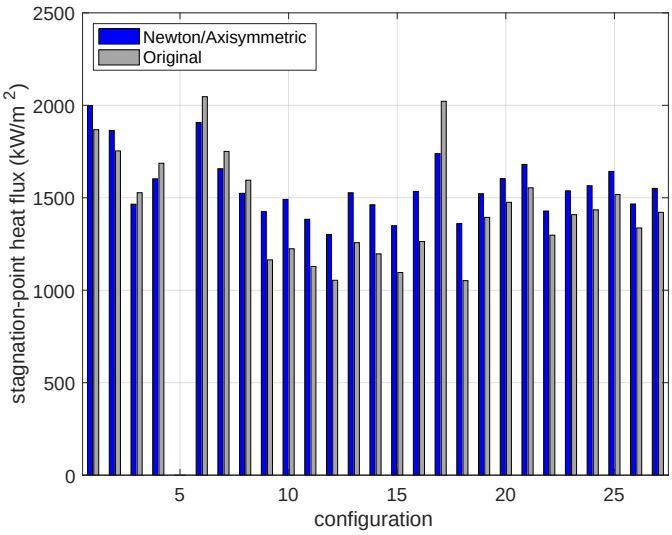

Figure 15. Comparison for stagnation-point heat flux, for all 27 configurations (# 5 missing).

stagnation point heat flux have become relatively reliable as they do not depend on complex geometrical aspects apart from the nose radius.

Significant differences were, however, observed for the maximum cone and flare heat fluxes, shown in Figs. 16 and 17, respectively.

The cone flux determined by the simplified model assumes a constant flux over the complete conic section, which is not true for the new model. There, the boundary layer growth is taken into account, and there is also no discrete location where the nose ends and the cone begins. For some configurations it was found that the flux behaviour, typically found on the nose would extend to the front part of the cone. Therefore, it would not be correct to use the flux at the nose-cone junction as the cone flux, but rather a location where the flux has "settled" to a value representative for the cone. So, for the sake of comparison in Fig. 16 the "new" cone flux is defined by this location and the corresponding heat flux.

The remaining differences in the cone heat flux results are caused mainly due to the type of the flow assumed over the conical surface. The original cone heat-flux equation from Ref. 1, Eq. (33), assumed laminar flow over the entire cone. The code developed in this paper uses two transition criteria, defined in

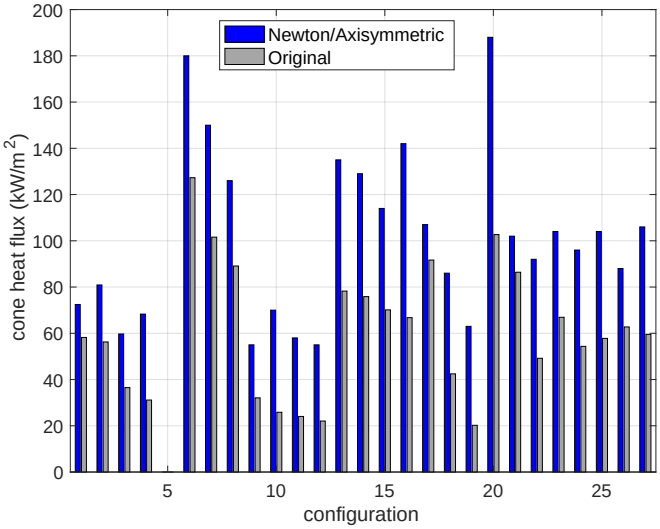

Figure 16. Comparison for cone heat flux, for all 27 configurations (# 5 missing). The location on the cone is determined based on the profile, away from the nose-cone junction.

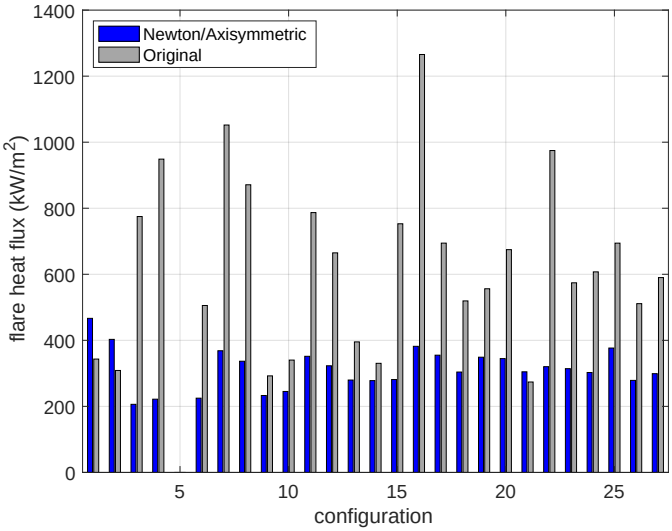

Figure 17. Comparison for flare heat flux, for all 27 configurations (# 5 missing).

Eqs. (22) and (23). To obtain a generally conservative estimate, the flow is set to turbulent once any of these criteria becomes satisfied. Thus for the majority of the cases, the transition did occur somewhere over the conical part, or even over the hemispherical nose. Since turbulent heat flux is typically several times higher compared to the laminar heat flux for the same conditions, this is also what causes such significant deviations in the results.

Figure 18 shows the cone heat flux for the nominal configuration according to the original data and also according to the presently developed method over the entire trajectory. Here, to illustrate the point made above, one simulation (turbulent) was run with a forced turbulent flow and the other with a forced laminar flow. It is clear that had the flow stayed laminar over the entire portion of the cone, the heat fluxes would have been very comparable with the original study. Here, the factor by which the heat flux increased is roughly 2, which corresponds to many cases presented in Fig. 16.

To assess which results are closer to the reality, one would have to analyse the reliability of the transition

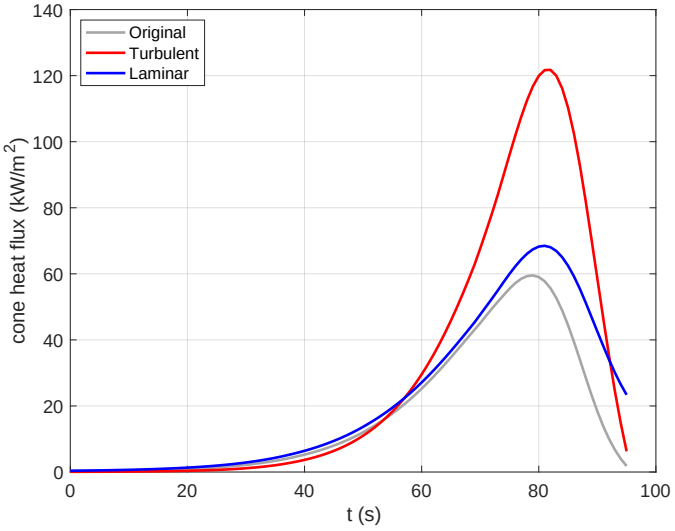

Figure 18. Time history of cone heat flux: comparison of laminar- and turbulent- flow models with original data (nominal configuration).

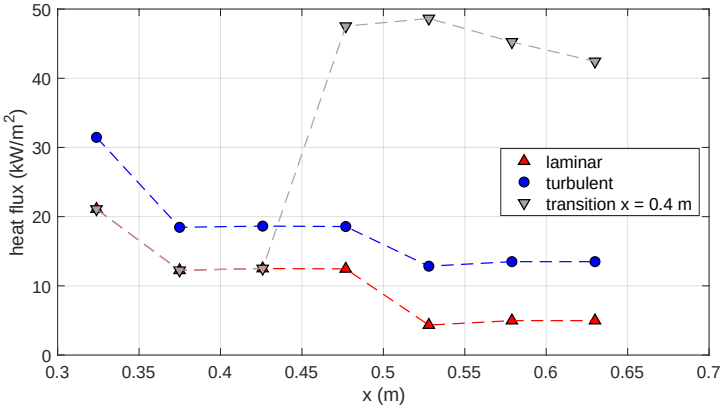

Figure 19. The effect of boundary-layer type and transition on the local heat flux at the cone.

prediction relations used in the present method. This will be further discussed in Section VI.

The flare results are also caused by the same discrepancy. Since, according to the present method, the transition occurs somewhere on the cone, it also means that the boundary layer grows significantly faster than it would have had the flow stayed laminar. Larger boundary layer over the flared part means that the heat flux over it will also be lower than it would have been had the transition occurred at the cone/flare junction, since the heat flux scales with $1/Re_\theta$. This further explains why there seems to be an association between the cases in the offsets in Figs. 16 and 17.

This is illustrated in Fig. 19. Here, the heat flux is shown over the conical part for the nominal configuration for tree cases: a fully laminar flow, a fully turbulent flow, and a flow which was artificially forced to undergo transition. Since the flow undergoing transition at 0.4 m has a smaller boundary layer θ_T compared to the flow, which was fully turbulent from the beginning of the geometry, the resulting turbulent heat-flux according to the Eq. (28) is larger.

Additional factor here is the fact that the original model of Sudmeijer and Mooij considers the interaction of the boundary layer and the shock at the cone/ flare junction. There is thus an additional term to the heating of the flare as a result of this interaction. The present method has had no such corrections implemented so far. The extent to which this is important for the heat flux results of the current configurations

has not been accurately determined yet.

E. Influence on the Shape Optimisation Results

The optimal shape from the original study of Sudmeijer and Mooij was based on evaluating the following performance indices:

1. x-location of centre of pressure (aerodynamic)
2. maximum cone-flare angle to avoid strong interaction (aerodynamic)
3. Maximum *g-load* (thermo-mechanical)
4. Maximum heat flux on the nose, cone and flare (thermo-mechanical)
5. Integrated heat load (thermo-mechanical)
6. Final velocity and altitude for stop criterion of Mach = 3 (trajectory)

Based on the discussion in Sub-section V.C, the 1^{st}, 3^{rd} and 6^{th} indices are not affected by the modified heat flux. As we already stated, the main focus of this paper is to evaluate the differences in heat flux, *i.e.,* index 4. Of course, the integrated heat load will change proportionally to the heat flux, since the flight time remains the same, and will therefore not be addressed separately.

In the previous sub-section we have already established (and explained) the differences in heat flux. Of the three locations, the stagnation-point heat flux compares the best in between the two models. So one would expect that when optimising for this criterion there will not be so much of a difference. However, two observations can be made. The first one concerns the variation between the concepts. The original model shows more variation and a larger difference between the minimum and maximum value ($q_{c,min}$ = 1,052 kW/m^2 (configuration #17) and $q_{c,max}$ = 2,047 kW/m^2 (#6), versus $q_{c,min}$ = 1,301 kW/m^2 (# 12) and $q_{c,max}$ = 1,998 kW/m^2 (#1) for the new model), but also the extrema appear for different concepts, the second observation. This extends to more of the configurations, *e.g.,* many of the "new" heat fluxes are a bit larger than the "old" ones, but, for instance, for concepts 3, 4, 6, 7, 8 and 17 this is reversed. So, there is not a regular bias, but this is geometry dependent, and not just based on the nose radius.

The consequence of the larger variation in fluxes is that it will be harder to establish a response surface, if that is going to be used for the subsequent optimisation. But, with the new model the variation is less non-linear (for lack of a better term), so this process would be easier. On the other hand, if the best concept would just be chosen from the set at hand, then obviously not the same one would be chosen (configuration #17 versus #12).

The variation and differences in the cone flux are even larger, although it seems that the differences are more consistent due to the fact that the (partial) turbulent flow on the cone will always result in a larger cone flux using the new model. There are still some discrepancies, though, that some geometries would show a decrease in cone flux with the old model (for instance, going from concept #15 to #16), whereas it would show an increase when the flux is evaluated with the new model.

One important aspect that was already mentioned in the previous sub-section is that when using the new model it is not straightforward when the nose ends and when the cone begins. For the data in Fig. 16 we explained that only when the cone flux settles to a profile that would meet the expectation of how this profile should be, *i.e.,* a more or less constant profile with only small gradients, we can define this location to be the beginning of the conic section. However, one could easily decide to stick to the geometric definition of the cone, *i.e.,* the junction of the nose cap with the cone. Doing so, however, could result in a very large flux value, because due to the combination of nose geometry and flow properties the nose seems to extend to the front part of the cone. In Fig. 20, the difference in flux while using either definition of the cone is shown. It is clear that these differences are substantial, and also not a constant offset. Would we have used the geometric definition of the cone, the difference between the old and the new model would be even larger: for the sake of completeness we have included this comparison in Fig. 21. In some of the cases the difference even amounts to well over 100%.

The last flux to analyse is the one on the flare. It has already be explained that the fluxes obtained with the new model will be lower, because transition of the boundary layer occurs earlier. As a consequence,

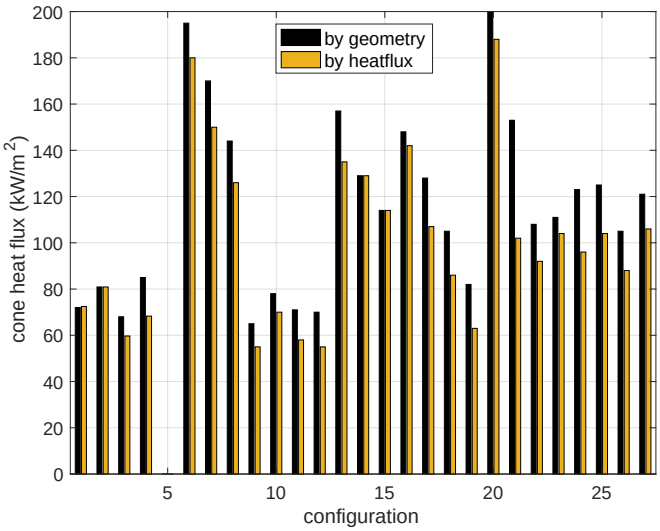

Figure 20. Comparison for cone heat flux, for all 27 configurations (# 5 missing), while using two different cone definitions.

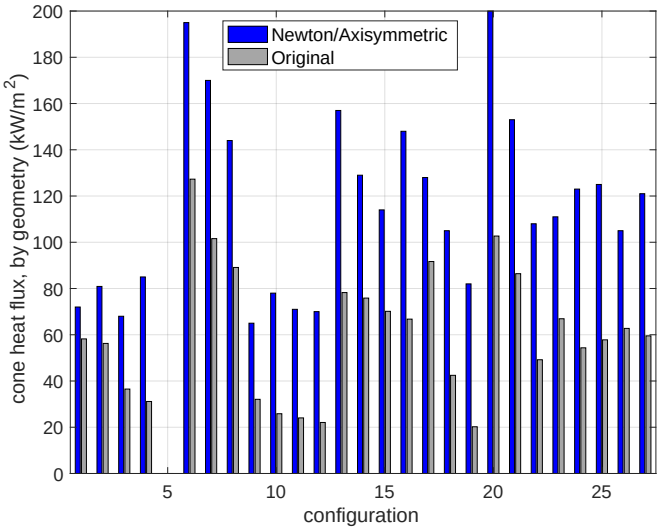

Figure 21. Comparison for cone heat flux, for all 27 configurations (# 5 missing), while using two different cone definitions.

there is also less variation in between the configurations, which would make it easier to construct response surfaces and subsequently optimise for minimum flare flux.

In conclusion, it is crucial to decide on the applied flux model, even in the conceptual design phase. Using simplified engineering models may be fast, but could drive the design in a less optimal direction. When the obtained heat fluxes are used for the conceptual design of thermal protection systems, the wrong choice of materials and/or wall thickness may be made. This would especially be true for the flare, where the found differences are substantial. But, independent of the selected model, one should always remain critical of the choices: even with the model proposed in this paper, one should be critical about the transition criterion that will be used, and even something relatively simple as "where does the nose end and the cone begin" may have an effect on the results.

VI. Discussion

As observed from Figs. 2 through 12, the adapted method provides an agreement with the CFD data with errors typically below 30%, but with locally large errors due to inaccuracies in the velocity field and incorrectly evaluated metric coefficients. This holds not only for the windward symmetry line, but also over the wings of the validation cases. This is deemed acceptable considering that the simulation is rapid compared to CFD and that its use is aimed at conceptual calculations only. It was shown that the time requirements are generally dictated by the speed of back-tracing and evaluation of the metric coefficients, both of which involve reconstruction of the surface streamlines. Currently, domain partitioning into sub-entities is used to accelerate this process, though these times could be far more significantly improved for structured meshes and if the code was parallelised.

Unlike most other rapid engineering methods, this technique provides heat-flux data at all mesh points on the windward side. Accuracy can only be increased to a certain extent, with a finer mesh and a smaller stagnation region, as that enhances the quality of the streamline reconstruction. However, the main source of errors remains the Newtonian approximation, so refining the discretisation beyond a certain level does not yield more accurate data.

When this method was applied to the shape optimisation study of Sudmeijer and Mooij from 2002, see Ref. 1, apart from the stagnation region, significant differences in the cone and flare heat fluxes were observed (see Figs. 16 and 17). These were found to mainly stem from the assumptions regarding the type of the flow present over the geometry. While the original study always assumed a laminar flow over the cone part and always a turbulent flow over the flare for the whole trajectory, the present method used two different criteria to calculate the location of the transition. This was demonstrated when the flow was forced to remain laminar for the present method in Fig. 18 for the nominal configuration, resulting in a heat flux, which matched the original data. In addition, the original study also included an empirical correction for a possible boundary-layer-shock interaction at the cone/flare junction, which might have had further increased the predicted flare heat flux.

This shows how important the considerations of transition are to design-optimisation studies. While expecting that the transition occurs at one specific point over the entire trajectory is usually not realistic without intentional tripping of the flow in some upstream location, also the transition-prediction relations used in the present method have shown significant offsets in the past.[9] For example, the "rule-of-thumb" of $Re_\theta/M_e = 100$ for the Space Shuttle became $Re_\theta/M_e = 285$ for the design of X33.[17] The Space-Shuttle transition-prediction method has been called very conservative, also because many times during the wind-tunnel experiments, based on which it was developed, the transition was caused rather due to freestream flow disturbances generated by the tunnel and not due to the supposed freestream conditions.[18] Thus, future shape-optimisation studies should also evaluate the sensitivity of the choice of the design on the transition criterion used.

Finally, several limitations of the present method should be listed, which will be addressed during further development of the code. These are:

1. The lack of reliable techniques to resolve the leeward inviscid flow field: currently, since a constant pressure coefficient is used for the leeward side, streamline tracing there is not possible. For simpler geometries, the leeward side could be resolved by a technique such as the Maslen method.

2. No considerations of the potential shock-boundary-layer interactions: in the current implementation, the effects of shock-boundary-layer interaction are neglected for any geometry. Since these interactions are not accounted for even in the original axisymmetric analogue method as implemented by Hamilton in Ref. 7, a separate study should be conducted to develop models for these corrections and a suitable method of their application. The importance of these effects on the optimisation study discussed above was, however, not yet evaluated.

3. No estimation of additional chemistry-related and radiative heat flux: the heat flux in the hypersonic regime will, in addition to the thermal-conductivity-related heat flux also consist of the diffusive heat flux and the radiative heat flux. The diffusive heat flux especially can represent a major contribution, and so techniques for its estimation, even if based on empirical approximations, should be developed to enhance the accuracy of the method.

4. Frequent inaccurate determination of the metric coefficient due to the very approximate velocity field: one of the main challenges this method faces remains the fairly inaccurate velocity field, especially

in regions with large geometric curvatures. In these cases, the streamlines resolved according to the Newtonian method are frequently inaccurate and even intersecting, leading to erroneous determination of the metric coefficient with the method of Parzhikar and thus usually a very low resolved heat flux. Further study should be performed to determine the adjustments or post-processing, which could be made either to the inviscid data or to the determination of the metric coefficient to eliminate this problem.

VII. Conclusions and Outlook

A rapid, hypersonic method based on the modified Newtonian technique for inviscid calculations and the axisymmetric analogue for viscous calculations has been developed, tested and applied. This method was developed as a conceptual approximation technique, when exploring and reducing the design space, before full CFD simulations of the selected concepts become practical.

From the comparison with the validation data of a blunted cone geometry and various Space Shuttle configurations, it has been shown that generally, this method can be expected to have errors of around 30%. Depending on the case geometry and thus the accuracy of the approximated velocity field, locally, the errors might exceed that value. A finer mesh and a definition of a smaller stagnation region might enhance the accuracy of the results, but beyond a certain resolution, the method is limited by the accuracy of the Newtonian approximation, making finer simulations costly and unnecessary. The time requirements for various portions of the simulations were evaluated, demonstrating its feasibility for conceptual design uses and indicating where the performance could be improved.

Afterwards, the original shape optimisation work of Mooij and Sudmeijer[1] for the DART module was re-visited. The geometry consists of a hemi-spherical nose extending into cone, which is followed by a flared geometry. The different shapes varied in nose radius, cone angle, flare angle, base radius and overall length. The heat fluxes of the configurations were re-computed with the present method. The trajectories of the original study were computed with inviscid forces coming from the Newtonian method only. Addition of the viscous forces computed by the present technique has, however, not significantly changed these trajectories. Thus, only the role of the altered heat flux on the performance indices was further investigated.

The original study assumed the transition to take place at one particular point on the geometry, the cone-flare junction, during the entire trajectory. On the other hand, the present technique employs a rather conservative estimate based on two criteria, which means that the transition occurred already at the cone part of the geometry. For that reason, the present method was found to result in the maximum cone heat fluxes often times several times higher than the original values. Due to the earlier transition, this also yielded smaller flare heat fluxes. When laminar flow over the cone part of the geometry was enforced in the present method, the match of the heat fluxes was acceptable, indicating that it was indeed the transition criterion which caused the offsets.

Which of these results are more realistic for the configurations here discussed depends on the accuracy of the considered transition criteria. This study thus also underlines how much delicate phenomena, such as transition, can affect the outcome of a design-optimisation study. Since it would not be practical to accurately compute the transition location for all the considered configurations and trajectories, a sensitivity analysis to the choice of the transition criterion might be useful when interpreting the results of such shape-optimisation studies in the future.

Compared with the original, simplified engineering model for the heat flux in the stagnation point, and on the cone and flare, the proposed model predicts fluxes that are significantly different. When used in a shape optimisation study, this will lead to alternate optimum configurations. The flux distribution over the different parts of the vehicle may lead to a change of thermal-protection system material and/or thickness, which, in turn, may affect the vehicle weight. This will change the trajectory and the induced thermo-mechanical loads. It is therefore important to have confidence in the applied models, even in the conceptual design phase, before one ends up with unnecessary design iterations. Validation of the results with full CFD solutions is therefore still a necessity at early stages of the design.

The present method has still several limitations, such its inability to resolve the leeward side, to estimate the other possible heat flux source (*e.g.,* the diffusive heat flux), to correct for inaccurate streamline tracing, and to apply corrections to regions undergoing boundary-layer-shock interactions. Further development of the code is planned such that it might be eventually possible to reliably and quickly do conceptual shape-optimisation studies.

References

[1]Sudmeijer, K.J. and Mooij, E., "Shape Optimisation for a Small Experimental Re-entry Module", AIAA-2002-5261, *AIAA/AAAF 11th International Space Planes and Hypersonic Systems and Technology Conference*, 2002.

[2]Cooke, J.C., "Axially Symmetric Analogue for General Three-Dimensional Boundary Layers", Reports and Memoranda No. 3200, British Aeronautical Research Council, 1961.

[3]Zoby, E.V. and Simmonds, A.L., "Engineering Flowfield Method with Angle-of-Attack Applications", *Journal of Spacecraft and Rockets*, Vol. 22, No. 4, 1985, pp. 398–404.

[4]Hamilton, H.H., DeJarnette, F.R., and Weilmuenster, K.J., "Application of Axisymmetric Analog for Calculating Heating in Three-Dimensional Flows", *Journal of Spacecraft and Rockets*, Vol. 24, No. 4, 1987, pp. 296-302.

[5]DeJarnette, F.R., Hamilton, H.H., Weilmuster, K.J. and Cheatwood, F.M., "A Review of Some Approximate methods Used in Aerodynamic Heating Analyses," AIAA-1985-0906, *AIAA 20th Thermophysics Conference*, Williamsburg, Virginia, June 19-21, 1985.

[6]DeJarnette, F.R. and Hamilton, H.H., "Aerodynamic Heating on 3-D Bodies Including the Effects of Entropy-Layer Swallowing", *Journal of Spacecraft and Rockets*, Vol. 12, No. 1, 1975, pp. 5-12.

[7]Hamilton, H.H., Weilmuenster, K.J., and DeJarnette, F.R., "Approximate Method for Computing Convective Heating on Hypersonic Vehicles Using Unstructured Grids", *Journal of Spacecraft and Rockets*, 2014, Vol. 51, No. 4, 2014, pp. 1288-1305.

[8]Parhizkar, H. and Karimian, S.M., "Application of Axisymmetric Analog to Unstructured Grid for Aeroheating Prediction of Hypersonic Vehicles", *International Journal of Numerical Methods for Heat and Fluid Flow*, Vol. 19, No. 3-4, 2009, pp. 501-520.

[9]Anderson, Jr., J.D., *Hypersonic and High-Temperature Gas Dynamics*, Second edition, AIAA Education Series, Reston, Virginia, 2006.

[10]Zarlin N. A., "Base Pressure Measurements on Sharp and Blunt 9 degree Cones at Mach Numbers from 3.5 to 9.2", Memorandum Report No. 1709, Ballistic Research Laboratory, Aberdeen, Proving Ground, 1965.

[11]Eckert E.R.C., "Engineering Relations for Heat Transfer and Friction in High-Velocity Laminar and Turbulent Boundary Layer Flows over Surfaces with Constant Pressure and Temperature", *Transactions of the American Society of Mechanical Engineering*, Vol. 78, No. 6, 1956, pp. 1273–1284.

[12]Sutton K. and Graves, R.A., "A general stagnation-point convective-heating equation for arbitrary gas mixtures", NASA Technical Report R-376, 1971.

[13]Johnson, C.B., Bushnell, D. M, "Power-Law Velocity-Profile-Exponent Variations with Reynolds Number, Wall Cooling and Mach Number in a Turbulent Boundary Layer", NASA Technical Note D-5752, 1970.

[14]Phadke, M.S., *Quality Engineering Using Robust Design*, Prentice-Hall, 1989.

[15]Krasnov, N.F., *Aerodynamics of Bodies of Revolution*, American Elsevier, New York, 1970.

[16]Simeonides, G., "Simple Theoretical and Semi-Empirical Convective Heat Transfer Predictions for Generic Aerodynamic Surfaces", YPA/1576/GS, ESA/ESTEC, 1995.

[17]Marqués P., Da Ronch A., *Advanced UAV Aerodynamics, Flight Stability and Control: Novel Concepts, Theory and Applications*, First edition, John Wiley & Sons, Inc., Chichester, United Kingdom, 2017.

[18]Miller C.G., "Development of X-33/X-34 Aerothermodynamic Data Bases: Lessons Learned and Future Enhancements", RTO AVT Symposium on Aerodynamic Design and Optimization of Flight Vehicles in a Concurrent Multi-Disciplinary Environment, Ottawa, Canada, October 18-21, 1999